Direct Photodetachment of F by mid-infrared few-cycle femtosecond laser pulses

Shearer, S. F. C., & Monteith, M. R. (2013). Direct Photodetachment of F by mid-infrared few-cycle femtosecond laser pulses. Physical Review A (Atomic, Molecular, and Optical Physics), 88(3), [033415]. DOI: 10.1103/PhysRevA.88.033415

Published in:
Physical Review A (Atomic, Molecular, and Optical Physics)

Document Version:
Publisher's PDF, also known as Version of record

Direct photodetachment of F^- by mid-infrared few-cycle femtosecond laser pulses

S. F. C. Shearer* and M. R. Monteith

Centre for Theoretical Atomic, Molecular and Optical Physics, Queen's University Belfast, Belfast, BT7 1NN, Northern Ireland

(Received 9 July 2013; published 13 September 2013)

The recent adiabatic saddle-point approach of Shearer *et al*. [Phys. Rev. A **84**, 033409 (2011)] is extended to multiphoton detachment of negative ions with outer *p*-state electrons. This theory is applied to investigate the strong-field photodetachment dynamics of F^- ions exposed to few-cycle femtosecond laser pulses, without taking into account the rescattering mechanism. Numerical calculations are considered for mid-infrared laser wavelengths of 1300 and 1800 nm at laser intensities of 7.7×10^{12}, 1.1×10^{13}, and 1.3×10^{13} W/cm^2. Two-dimensional momenta saddle-point spectra exhibit a distinct distribution in the shape of a "smile" in the complex-time plane. Electron momentum distribution maps of direct electrons are investigated. These produce a distinct pattern of above-threshold detachment (ATD) concentric rings due to constructive and destructive quantum interference of electrons detached from their parent ions. Probability detachment distributions presented, capturing the influence of saturation effects that are found to become more significant with increasing laser intensity at a fixed wavelength. ATD photoangular distributions as functions of laser intensity and wavelength near channel closings are also investigated and found to be sensitive to initial-state symmetry. Nonmonotonic structures observed in the ejected photoelectron energy spectra are attributed to interference effects from coherent electronic wave packets. Additionally the profiles of all the photoelectron emission spectra show strong dependence on the carrier-envelope phase, indicating that it is a reliable parameter for characterizing the wave form of the pulse.

DOI: 10.1103/PhysRevA.88.033415 PACS number(s): 32.80.Rm, 32.80.Gc

I. INTRODUCTION

Optical control of laser-induced photodetachment of halide negative ions by few-cycle pulses has become a subject of significant interest in the domain of strong-field atomic physics in the last few years. Historically experimental [1–5] and theoretical studies [6–13] on multiphoton detachment of halide negative ions have focused on periodic multicycle laser pulses defined in terms of frequency, amplitude, and polarization. Lately advancements in laser technology have prompted theoreticians to probe the process of multiphoton detachment of halide negative ions by intense phase-controlled few-cycle infrared laser pulses [14–18]. The additional parameters required to characterize a few-cycle pulse are the carrier-envelope phase (CEP) and the cycle number. Variation of these control parameters determines the behavior of the electric field wave form of the pulse and thus offers the potential to significantly enhance the possibilities for achieving coherent control over the subsequent photodetachment dynamics.

At present one of the most successful analytical approaches developed for the description of strong-field photodetachment of negative ions is the adiabatic saddle-point method of Gribakin and Kuchiev [6] (GK). The original GK model was developed for linearly periodic laser pulses and consists of neglecting the action of the ionic Coulombic field on the photoelectron. The final electron state may then be represented by the Volkov wave function [19]. This approximation is well justified because it accurately includes the short-range polarization interaction between the outer bound electron and the core of the parent ion. The GK theory provides an intuitive description of photodetachment, relating it to a coherent superposition of electron trajectories in the continuum. This leads to a quantum interference signature. Analytically the signature arises from the superposition of two complex saddle-point contributions per oscillation period that is intrinsically included in the final expression describing the photodetachment rate.

Such quantum interference effects have been observed and analyzed in experimental studies on strong-field photodetachment of halogen negative ions, including F^-, exposed to monochromatic linearly polarized femtosecond infrared laser fields in the multiphoton regime [1,4]. This work demonstrated that the GK method was qualitatively able to reproduce the photoelectron spectra accurately without taking into account the rescattering mechanism in the low photon energy range investigated.

Recently, increasing interest in coherent control of direct photodetachment of negative ions in intense ultrashort laser fields prompted us to extend the GK approximation, to consider wave-form-controlled few-cycle linearly polarized pulses [20,21] of H^- ions. In that work we considered direct electrons in a monochromatic laser field driven by a few-cycle laser pulse with a sine-squared pulse consisting of N optical cycles and showed that there are exactly $2(N+1)$ ionization times over the duration of the laser pulse and hence $2(N+1)$ quantum orbits in the final continuum state [20,21]. The $2(N+1)$ quantum orbits are distinct and thus each needs to be calculated separately. However, the orbits that make the most dominant contributions arise from the saddle-point contributions that are closest to the center of the pulse where the electric field is strongest. The contributions of all the orbits add coherently to the photodetachment amplitude leading to interference of the corresponding wave packets. The resulting photoelectron emission spectra are dominated by these quantum interference packets [20,21] which may enhance or suppress a particular transition depending on the relative phase difference of the alternative photodetachment transition amplitudes.

In this paper we adapt our approach in [20,21] to study direct photodetachment of F^- negative ions in mid-infrared

*f.shearer@qub.ac.uk

short-cycle (femtosecond) laser fields (i.e., pulse duration between 17 and 24 fs) in the multiphoton regime. A detailed analysis of the influence of laser intensities (7.7×10^{12}, 1.1×10^{13}, and 1.3×10^{13} W/cm^2), wavelengths (1300 and 1800 nm), and various values of CEP (measured in radians) with a four-cycle pulse on the (i) momentum saddle-point distributions, (ii) photoelectron momentum distribution maps, (iii) three-dimensional (3D) differential detachment probabilities, (iv) photoangular distributions (PADs), and (v) electron energy spectra is carried out.

The behavior of the momentum saddle-point density distributions is found to be highly correlated with laser intensity and wavelength and the CEP. Investigation confirms that the distribution profiles of all photoemission spectra considered may be controlled by the CEP. Conversely the spectra reveal phenomena of the photodetachment dynamics on the short femtosecond time scale considered here. Above-threshold detachment (ATD) rings at fixed energy are a distinguishing feature of the momentum distribution maps which result from quantum interference effects. Analysis of the calculated detachment probability distributions indicates that saturation effects start to play a role in the photodetachment structure and dynamics as the laser intensity is increased. Calculations show that the ATD photoangular distributions are dependent on the initial-state symmetry of the active electron and that the topological structures of the distributions are determined by whether an odd or even number of photons is absorbed. The PADs also exhibit a strong sensitivity to laser wavelength and intensity. A signature of quantum interference phenomena in the time domain is observed in the electron energy spectra as nonmonotonic structures. The calculations are compared with existing available theoretical and experimental data [1,4,11,20–24].

This paper is organized as follows. In Sec. II we extend the approach in [20,21] from the case of initial s-state symmetry to initial p-state symmetry, to study photodetachment of F^- ions by few-cycle laser pulses. We neglect the rescattering mechanism of the detached electron from the parent ion since our theory is restricted to the low-energy part of the spectrum, where its structure is strongly correlated with the orbital quantum number l of the initial ground state. The influence of depletion in the ground state is also ignored. In our calculations we use detachment probabilities to account for the finite duration of the few-cycle laser pulse, instead of detachment rates based on a quasienergy approach which assumes the presence of a monochromatic laser field. In Sec. III we discuss the results of our numerical calculations and analyze the threshold behavior of multiphoton detachment near channel closings. Finally in Sec. IV we present our conclusions. Note that throughout this paper atomic units are used unless otherwise stated.

II. THEORY

We consider detachment for F^- having a p outer electron by an ir laser field

$$\mathbf{F}(t) = -\frac{d\mathbf{A}}{dt}, \tag{1}$$

where we assume the laser is polarized along the $\hat{\mathbf{z}}$ axis whose time-dependent vector potential is given by

$$\mathbf{A}(t) = A(t)\hat{\mathbf{z}} = A_0\left[\sin^2\left(\frac{\omega t}{2N}\right)\sin(\omega t + \alpha)\right]\hat{\mathbf{z}}. \tag{2}$$

Here ω is the frequency of the pulse, N is the number of optical cycles in the pulse, and α is the CEP. The peak value A_0 of the vector potential $\mathbf{A}(t)$ is related to the peak laser intensity I_0 by

$$A_0 = \sqrt{I_0/I_{\text{a.u.}}}/\omega = F_0/\omega, \tag{3}$$

where $I_{\text{a.u.}} = 3.515 \times 10^{16}$ W/cm^2 and F_0 is the peak value of the electric field strength. It is useful to note that the component of the vector potential $\mathbf{A}(t)$ of the sine-squared N-cycle laser pulse in the $\hat{\mathbf{z}}$ direction is composed of three quantized frequency components and thus may be written in the form

$$A(t) = \frac{A_0}{4}[2\sin(\omega_1 t + \alpha) - \sin(\omega_2 t + \alpha) - \sin(\omega_3 t + \alpha)], \tag{4}$$

where $\omega_1 = \omega$, $\omega_2 = \omega(1 + \frac{1}{N})$ and $\omega_3 = \omega(1 - \frac{1}{N})$. The photoelectron spectrum for the N-cycle laser pulse in the laser field $\mathbf{F}(t)$ is determined by the differential detachment probability

$$dw = 2|A_{\mathbf{p}}|^2\frac{d^3p}{(2\pi)^3}, \tag{5}$$

where the factor of 2 is included to take account of the electron spin projections. Inspection of Eq. (5) for the differential detachment probability reveals that the conservation of energy is not incorporated via a δ function, as is the case in the differential detachment rate for periodic multicycle pulses. From [20] the photodetachment amplitude $A_{\mathbf{p}}$ of electron ejection with momentum $\mathbf{p}$ and pulse duration $\tau = 2\pi N/\omega$ may be written in the form

$$A_{\mathbf{p}} = \int_0^\tau \left[E_0 - \frac{1}{2}(\mathbf{p} + \mathbf{k}_t)^2\right]\tilde{\Phi}(\mathbf{p} + \mathbf{k}_t) \times \exp\left[\frac{i}{2}\int^t (\mathbf{p} + \mathbf{k}_{t'})^2 dt' - iE_0 t\right]dt, \tag{6}$$

where $\mathbf{k}_t$ is the classical electron momentum due to the field, given by

$$\mathbf{k}_t = -\int^t \mathbf{F}(t')dt', \tag{7}$$

and

$$\tilde{\Phi}(\mathbf{q}) = \int e^{-i\mathbf{q}\cdot\mathbf{r}}\Phi_0(\mathbf{r})d\mathbf{r} \tag{8}$$

is the Fourier transform of $\Phi_0(\mathbf{r})$. The general asymptotic form of $\Phi_0(\mathbf{r})$ is

$$\Phi_0(\mathbf{r}) \simeq \frac{A}{r}\exp(-\kappa r)Y_{lm}(\hat{\mathbf{r}}), \tag{9}$$

where $\hat{\mathbf{r}} = \mathbf{r}/\mathbf{r}$ is the unit vector and A and κ are the asymptotic parameters corresponding to the bound-state wave function. Here l and m represent the angular momentum quantum numbers of the electron in the initial state. $\Phi_0(\mathbf{r})$ has a well-defined asymptotic form since our calculation is within the length-gauge formalism. Using [25] the following asymptotic

form of $\Phi_0(\mathbf{q})$ of the valence electron of the negative ion for $q \to \pm i\kappa$ is obtained:

$$\Phi_0(\mathbf{q}) \simeq \frac{4\pi A(\pm)^l Y_{lm}(\hat{\mathbf{p}})}{q^2+\kappa^2}, \tag{10}$$

where $(\pm)^l \equiv (\pm 1)^l$ corresponds to $q \to \pm i\kappa$. Thus

$$\Phi_0(\mathbf{p}+\mathbf{k}_t) \simeq \frac{4\pi A(\pm)^l Y_{lm}(\hat{\mathbf{p}})}{(\mathbf{p}+\mathbf{k}_t)^2+\kappa^2}. \tag{11}$$

The integrand in Eq. (6) contains a rapidly ocillating exponent $\exp[if(t)]$, where

$$f(t) = \frac{1}{2}\int^t (\mathbf{p}+\mathbf{k}_{t'})^2 dt' - E_0 t. \tag{12}$$

The positions of the saddle points are given by a solution of

$$(\mathbf{p}+\mathbf{k}_t)^2 + \kappa^2 = 0, \tag{13}$$

where κ parametrizes the binding energy $|E_0| \equiv \kappa^2/2$ of the corresponding bound state. In accordance with the theory of adiabatic transitions only the saddle points in the upper half plane of complex t are taken into account in Eq. (13). The saddle points correspond physically to the coherent emission of the photoelectron at different complex moments of time where the transition from the bound state into the Volkov state takes place. For a short laser pulse with N optical cycles and a sine-squared envelope as considered here, Eq. (13) takes the form

$$\left[\mathbf{p} + \frac{\mathbf{F}}{\omega}\sin^2\left(\frac{\omega t}{2N}\right)\sin(\omega t+\alpha)\right]^2 + \kappa^2 = 0. \tag{14}$$

Reducing the saddle-point equation (14) to scalar form and setting $\phi = \omega t$ yields

$$p^2 + \frac{2pF\cos\theta}{\omega}\sin^2\left(\frac{\phi}{2N}\right)\sin(\phi+\alpha) + \frac{F^2}{\omega^2}\sin^4\left(\frac{\phi}{2N}\right)\sin^2(\phi+\alpha) + \kappa^2 = 0, \tag{15}$$

where θ is the angle between the photoelectron momentum $\mathbf{p}$ and the field $\mathbf{F}$. As in [20,21], numerical solution of Eq. (15) for F^- yields $2(N+1)$ complex roots, where $2N$ of the roots arise from the the laser frequency ω_1 and the additional two roots arise from the frequencies ω_2 and ω_3, respectively. Using the saddle-point method we can evaluate the direct transition amplitude for the low-energy part of the spectrum to obtain

$$A_{\mathbf{p}} = -(2\pi)^{3/2} A \sum_{\mu=1}^{2(N+1)} (\pm)^l Y_{lm}(\hat{\mathbf{p}}_\mu)\frac{\exp[if(t_\mu)]}{\sqrt{-if''(t_\mu)}}, \tag{16}$$

where the sum is over all the saddle points t_μ and $\hat{\mathbf{p}}_\mu$ is the unit vector in the direction of the complex momentum $\mathbf{p}+\mathbf{k}_t$ evaluated at the saddle points. Explicit expressions for $f(t_\mu)$ and $f''(t_\mu)$ in Eq. (16) for the sine-squared N-cycle laser pulse are given in [20]. As in [6] the spherical harmonics used in Eq. (16) are defined as

$$Y_{lm}(\Theta,\varphi) = \frac{1}{\sqrt{2\pi}} e^{im\varphi}(-1)^{(m+|m|)/2}\left[\frac{2l+1}{2}\frac{(l-|m|)!}{(l+|m|)!}\right]^{1/2} \times P_l^{|m|}(\cos\Theta). \tag{17}$$

Equation (17) may be geneneralized to calculate $Y_{lm}(\hat{\mathbf{p}}_\mu)$ for complex vectors where

$$\cos\Theta = \frac{(\mathbf{p}+\mathbf{k}_t)\cdot\mathbf{F}}{\sqrt{(\mathbf{p}+\mathbf{k}_t)^2 F}} = \left(1+\frac{p_\perp^2}{\kappa^2}\right)^{1/2}. \tag{18}$$

The last equality in Eq. (18) is valid at the saddle points and $p_\perp = p\sin\theta$ is the component of $\mathbf{p}$ perpendicular to $\mathbf{F}$. We note here that the component of momentum of the detached electron parallel to the field is denoted by $p_{||} = p\cos\theta$. The real physical angle θ should not be confused with the complex angle Θ from Eqs. (17) and (18). The azimuthal angle φ is the same in both cases.

The differential detachment probability in Eq. (5) may be rewritten in the form

$$\frac{dw}{dE_e d\Omega} = \frac{2p|A_{\mathbf{p}}|^2}{(2\pi)^3}. \tag{19}$$

Integrating Eq. (19) over the electron energy dE_e yields the photoangular distribution

$$\frac{dw}{d\Omega} = \int_0^\infty \frac{dw}{dE_e d\Omega} dE_e. \tag{20}$$

Similarly integrating Eq. (19) over the differential solid angle $d\Omega = \sin d\theta d\varphi$ (where θ and φ are the scattering and azithmual angles) of the final momentum of the photoelectron yields the energy spectrum

$$\frac{dw}{dE_e} = 2\pi\int_0^\pi \frac{dw}{dE_e d\Omega}\sin\theta d\theta, \tag{21}$$

and the total detachment probability is obtained by integrating Eq. (21) over the electron energy to obtain

$$w = \int_0^\infty \frac{dw}{dE_e} dE_e. \tag{22}$$

We now apply this theory to study the above-threshold detachment spectra of the negative F^- ion. Since the valence electron in the F^- ion in the p ground state has orbital momentum $l=1$ the detachment probability should be summed over contributions from the initial-state components with $m = 0,\pm 1$. The effect of fine structure splitting is taken into account by a statistical averaging of channels with the two different spin-orbit sublevels corresponding to $j = l \pm \frac{1}{2}$ of the closed p shell of F^- of the final doublet atomic states $^2P^0_{1/2}$ and $^2P^0_{3/2}$, respectively. These channels are characterized by different binding energies $|E_0|_j \equiv \kappa_j^2/2$ dependent on whether $j = 1/2$ or $3/2$, respectively. Using the fine structure splitting energy of 0.0019 a.u. equivalent to 50.1 meV taken from [26] we assign the binding energy of 0.1268 a.u. (3.451 289 eV) to the upper $^2P^0_{1/2}$ spin-orbit sublevel and a binding energy of 0.1249 a.u. (3.401 189 eV) to the lower $^2P^0_{3/2}$ sublevel. Thus the average photon detachment probability for the j sublevel of the F^- ion is given by

$$\frac{dw^j}{dE_e d\Omega} = \sum_j \sum_{m=-1}^{+1} \frac{2j+1}{2L+1}\frac{dw_{lm}^{(j)}}{dE_e d\Omega}, \tag{23}$$

where $j = 1/2, 3/2$ are the two possible values of the total angular momentum of the residual atom, $L=1$ is its total orbital momentum, $dw_{lm}^{(j)}/dE_e d\Omega$ is calculated from Eq. (19) for the

jth sublevel, and the corresponding differential detachment probability is denoted by

$$dw^j = \sum_j \sum_{m=-1}^{+1} \frac{2j+1}{2L+1} dw_{lm}^{(j)}, \tag{24}$$

where the notation $dw_{lm}^{(j)}$ has been introduced specifically to identify that the jth sublevel is synonymous with the formula defined earlier in Eq. (5). In this paper our calculations use Eq. (23) to calculate the differential detachment probabilities for $j = 1/2$ since we consider the detachment of $p_{1/2}$ electrons from F^- ions, and the asymptotic parameter A of the p ground state given in Eq. (9) for the F^- ion is taken from [27].

III. NUMERICAL RESULTS AND DISCUSSION

In our calculations we consider a laser pulse with $N = 4$ optical cycles. We consider pulses with three peak intensities 7.7×10^{12}, 1.1×10^{13}, and 1.3×10^{13} W/cm^2 for each of two laser wavelengths $\lambda = 1300$ and 1800 nm (corresponding to laser frequencies $\omega = 0.035\,05$ and $0.025\,32$ a.u. and photon energies of 0.954 and 0.689 eV, respectively) with CEP values of $\alpha = 0$, $\pi/2$, and $3\pi/2$, respectively. The corresponding saddle points of Eq. (15) in each case for both (i) 2D momentum distributions and (ii) differential detachment probability, energy, and angular distributions are estimated graphically from the 3D surface plots of $|f'(\phi)|^{-1/2}$ and as such are identified as infinities instead of zeros.

The momentum surface plots are calculated from Eq. (15), where we take p_x (i.e., $p_\perp$) $= p \sin\theta$ and p_z (i.e., $p_{||}$) $= p \cos\theta$. These yield ten approximate, momentum complex saddle points which are the saddle-point solutions to Eq. (15). These graphical solutions are refined by employing the Newton-Raphson method to ensure that we employ a higher degree of accuracy in our calculations. The numerical calculation for 2D momentum (p_x, p_z) distributions of photoelectron spectra requires refining each of the ten roots individually over a range of p_x and a range of p_z. For our calculations we consider low-energy photoelectron momenta p_x and p_z ranging from -1.0 to $+1.0$ a.u., i.e., $E_e \leqslant 0.5$ a.u. for $\lambda = 1300$ nm, where $E_e = (p_x^2 + p_z^2)/2$. A step size of 0.01 a.u. for p_x and p_z was taken in the calculation. Similarly for $\lambda = 1800$ nm we take p_x and p_z ranging from -1.2 to $+1.2$ a.u., i.e., $E_e \leqslant 0.72$ a.u., taking a step size of 0.012 a.u. for both the x and z components of the momentum p. The refined roots are used to calculate the 2D photoelectron momentum distributions in Figs. 2 and 3.

Similarly, energy and angular surface plots are required to guesstimate initial values of the energy and angular saddle points. As in the case of the momentum surface plots the energy and angular surface plots yield ten approximate complex roots. These are the corresponding saddle-point solutions of Eq. (15). Application of the Newton-Raphson method then involves refining each of the ten graphically estimated roots individually for a range of angles θ between the direction of the field and the momentum $\mathbf{p}$ of the detached electron. In our calculations we consider θ in the range $0 \leqslant \theta \leqslant 180^\circ$ taking a step size of 1° and the photoelectron energies E_e in the range $0.05\omega \leqslant E_e \leqslant 10\omega$. The momentum values p for each frequency ($\omega = 0.035\,05$ a.u., $0.025\,32$ a.u.) ranging from the corresponding threshold values (0.0592 and 0.0503 a.u.) to maximum values (0.8373 and 0.7116 a.u.), respectively, are obtained by taking $p = \sqrt{2E_e}$ for equally spaced energies $E_{ej} = (\omega/20)j$ with $j = 1,2,\ldots,200$. The refined Newton-Raphson roots are then used in Eq. (16) for the transition amplitude to calculate the emission spectra for the 3D photodetachment probabilities, PADs, and photoelectron energy spectra, respectively, in Figs. 4–7, respectively.

A. Momentum saddle-point distributions

In Fig. 1 we show ten momentum saddle points that are solutions of Eq. (15) with $p_x = p\sin\theta$ and $p_z = p\cos\theta$ for a four-cycle pulse at a fixed laser intensity of 1.3×10^{13} W/cm^2 with fixed wavelengths of $\lambda = 1300$ and 1800 nm and CEP values of $\alpha = 0$, $\pi/2$, and $3\pi/2$, respectively. Figures 1(a)–1(c) depict the saddle points for five values of p_x in the range $-1 \leqslant p_x \leqslant 1$ and five values of p_z in the range $-1 \leqslant p_z \leqslant 1$ for $\lambda = 1300$ nm corresponding to $E_e \leqslant 0.5$ a.u. Similarly, Figs. 1(d)–1(f) depict saddle points for five values of p_x in the range $-1.2 \leqslant p_x \leqslant 1.2$ and five values of p_z in the range $-1.2 \leqslant p_z \leqslant 1.2$ for $\lambda = 1800$ nm corresponding to $E_e \leqslant 0.72$ a.u. That is, to ease visual analysis of the computed data, the momentum saddle points shown in Fig. 1 are a subset (10 saddle points) $\times$ (5 photoelectron momenta p_x) $\times$ (5 photoelectron momenta p_z) of the number of saddle points used in our calculations in Figs. 2 and 3. The actual number of saddle points used in Figs. 2 and 3 are calculated from an array of size (10 saddle points) $\times$ (200 p_x momentum components) $\times$ (200 p_z momentum components). As in [20,21] for H^- ions the saddle points are distributed in the shape of a "smile." Each group of red circles or blue crosses represents the position of a saddle point for the given range of photoelectron momenta described above. Alternating color has been used to make each saddle point distinguishable from the others as consecutive saddle points for the given range of photoelectron momenta (p_x, p_z) considered lie so closely together.

The data in Fig. 1 show that the positions of the saddle points in the complex plane are critically dependent on the wavelength and CEP at a fixed intensity. In particular it is noted from Figs. 1(a)–1(c) that as the wavelength increases for both a fixed intensity and fixed CEP the saddle points move closer to the real axis as shown in Figs. 1(d)–1(f). Further calculations not shown here also show that as the intensity is decreased, from 1.3×10^{13} to 1.1×10^{13} to 7.7×10^{12} W/cm^2 for fixed wavelengths 1300 and 1800 nm, with fixed CEP values considered as above, the saddle points move further away from the real axis. It is observed that for a fixed intensity and fixed wavelength an increase in CEP moves the roots along the smile. It is noted that for $\theta = 0$ the electron is likely to be detached parallel to the field (i.e., when $\theta = 0$ or π) rather than perpendicular to it (i.e., when $\theta = \pi/2$).

We now enquire into the relative importance that contributions from different saddle points will have for the transition amplitude. For this purpose we explore the behavior and location of various individual saddle points in Fig. 1. For both wavelengths and intensities considered here, our calculations show that for a CEP of $\alpha = 0$, root 5 is closest to the real axis, for $\alpha = \pi/2$, roots 5 and 6 are equally close to the real axis,

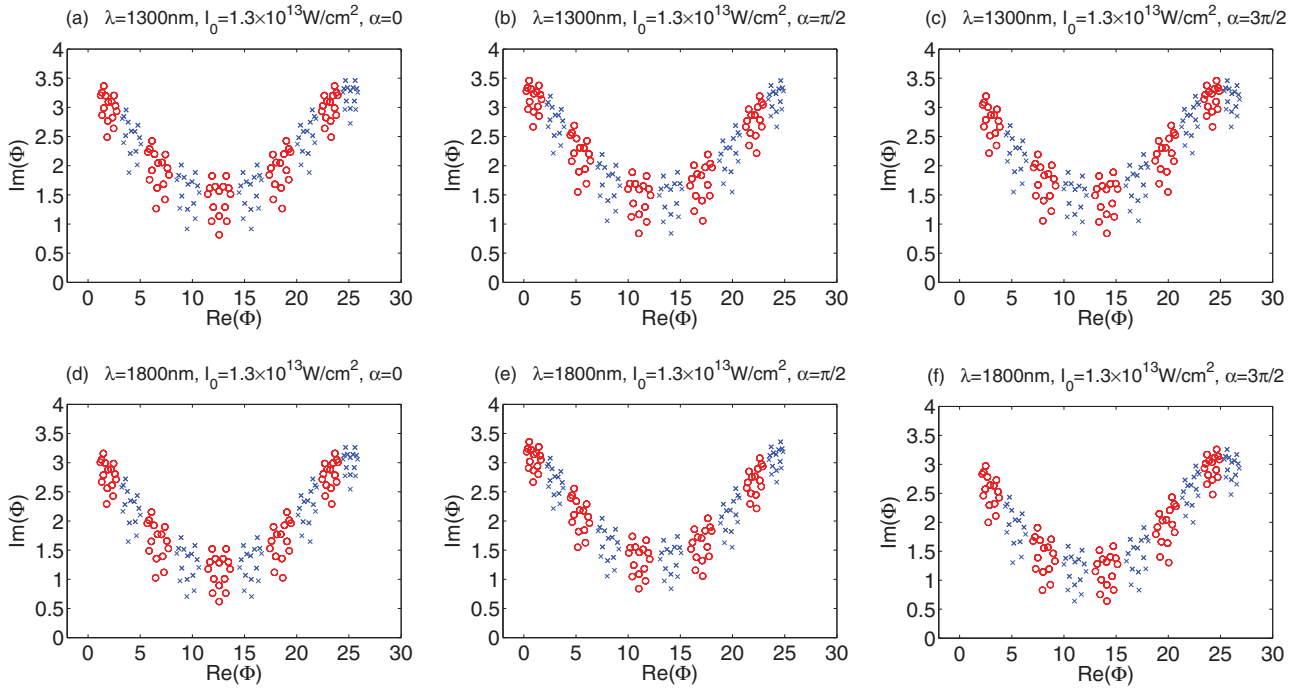

FIG. 1. (Color online) Momentum complex-time saddle points for the four-cycle pulse at a laser intensity of 1.3×10^{13} W/cm^2. The panels in each row represent wavelengths of 1300 and 1800 nm. The panels in each column correspond to the CEP $\alpha = 0$, $\pi/2$, and $3\pi/2$. In (a), (b), and (c) each group of points represent the positions of a saddle point for a range of photoelectron momenta p_x and p_z ranging from -1.0 to $+1.0$ a.u. for $\lambda = 1300$ nm. In (d), (e), and (f) each group of points represent the positions of a saddle point for a range of photoelectron momenta p_x and p_z ranging from -1.2 to $+1.2$ a.u. for $\lambda = 1800$ nm. In each group, the points closest to the real axis correspond to the smallest values of photoelectron momenta.

and for $\alpha = 3\pi/2$, roots 4 and 5 are closest to the real axis. The location of these roots predicts precisely which roots will make the most significant contribution to the transition amplitude as the CEP is varied. Further inspection of the saddle-point distributions indicates that the symmetrical properties of the distribution are highly sensitive to variation of the CEP. The

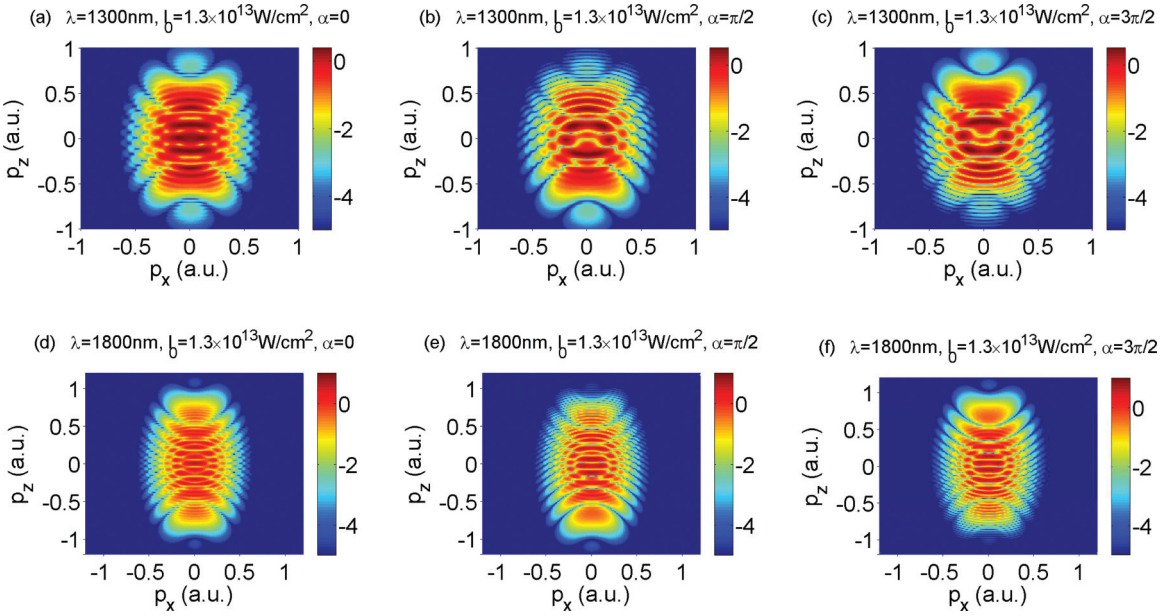

FIG. 2. (Color online) (a), (b), and (c) show the logarithm of the 2D momentum distributions (p_x, p_z) of photoelectrons detached from F$^-$ at a laser intensity 1.3×10^{13} W/cm^2 with a sin^2 pulse duration of four optical cycles. The panels in each row correspond to a CEP of $\alpha = 0$, $\pi/2$, and $3\pi/2$, respectively, at a laser wavelength of 1300 nm. (d), (e), and (f) are as in (a), (b), and (c) except now the laser wavelength is 1800 nm.

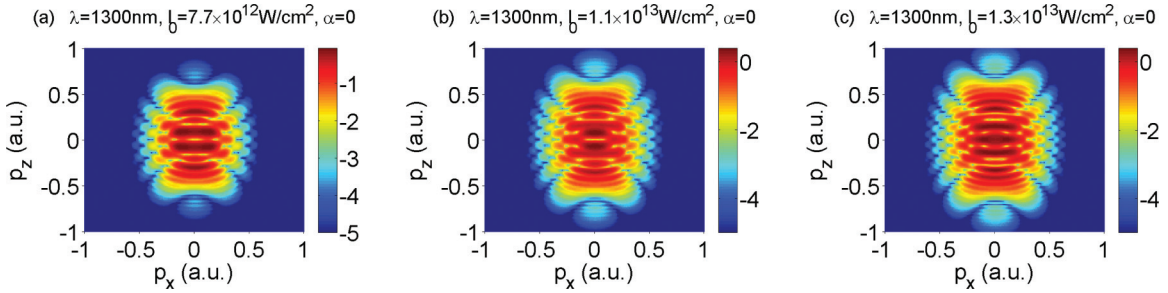

FIG. 3. (Color online) (a), (b), and (c) show the logarithm of the 2D momentum distributions (p_x, p_z) of photoelectrons detached from F^- at a laser wavelength of 1300 nm and $\sin^2$ total pulse duration of four optical cycles at intensities of 7.7×10^{12}, 1.1×10^{13}, and 1.3×10^{13} W/cm^2, respectively, calculated at a CEP of $\alpha = 0$.

simulations in Fig. 1 show that the saddle-point distributions are symmetric for $\alpha = \pi/2$ and asymmetric for $\alpha = 0$ and $\alpha = 3\pi/2$. These results indicate that the CEP controls the photodetachment dynamics of the momentum spectra.

Similar saddle-point distributions not reported here are also obtained for a suitable range of photoelectron energies and angles directly from Eq. (15), for array sizes of (10 saddle points) × (200 photoelectron energies) × (180 scattering angles). These we use to calculate the photodetachment probability distributions, PADs, and photoelectron energy spectra in Figs. 4, 5, 6, and 7 respectively. The CEP is also found to strongly control the influence of individual saddle points on the photodetachment dynamics of the differential detachment probability distributions, PADs, and photoelectron energy spectra.

B. Photoelectron momentum distributions maps

In Fig. 2 we present the 2D momentum distribution maps of the photoelectron spectra for F^- with a laser pulse duration of four optical cycles at a fixed laser intensity of 1.3×10^{13} W/cm^2 with laser wavelengths of 1300 and 1800 nm, respectively, and three different values of the CEP $(\alpha = 0, \pi/2, 3\pi/2)$. The 2D momentum distribution maps have been calculated from the logarithm of the differential detachment probabilities of F^-.

The most striking feature of the momentum distributions in Fig. 2 is the richly structured interference pattern originating from the oscillatory behavior of the few-cycle laser pulse and the modulation of wave-packet dynamics. A distinctive feature of the interference pattern recorded in the momentum spectra is the series of concentric rings emanating from the center of each distribution in Figs. 2(a)–2(f). These ring structures are centered at zero momentum and correspond to characteristic above-threshold detachment peaks. The innermost rings in Figs. 2(a), 2(b), and 2(c) correspond to a six-photon detachment channel and Figs. 2(d), 2(e), and 2(f) correspond to an 11-photon detachment channel. Additional interference rings are produced at the higher wavelength (and at higher intensities as shown in Fig. 3) due to the

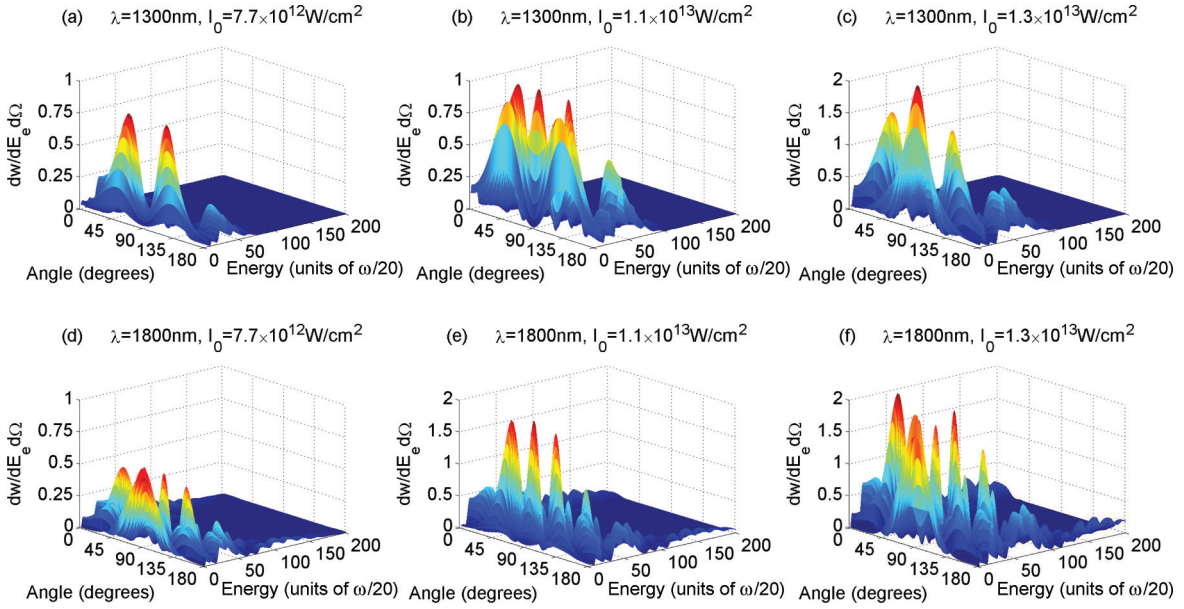

FIG. 4. (Color online) Differential detachment probabilities $dw/dE_e d\Omega$ for the four-cycle pulse calculated with a CEP of $\alpha = 0$. The panels in each row represent intensities of 7.7×10^{12}, 1.1×10^{13}, and 1.3×10^{13} W/cm^2. The panels in each column correspond to laser wavelengths of 1300 and 1800 nm, respectively. These distributions include contributions from the $m = 0$, -1, and $+1$ states. The effect of fine structure splitting has been taken into account. The energy axis in each plot shows the photoelectron energy in units of $\omega/20$.

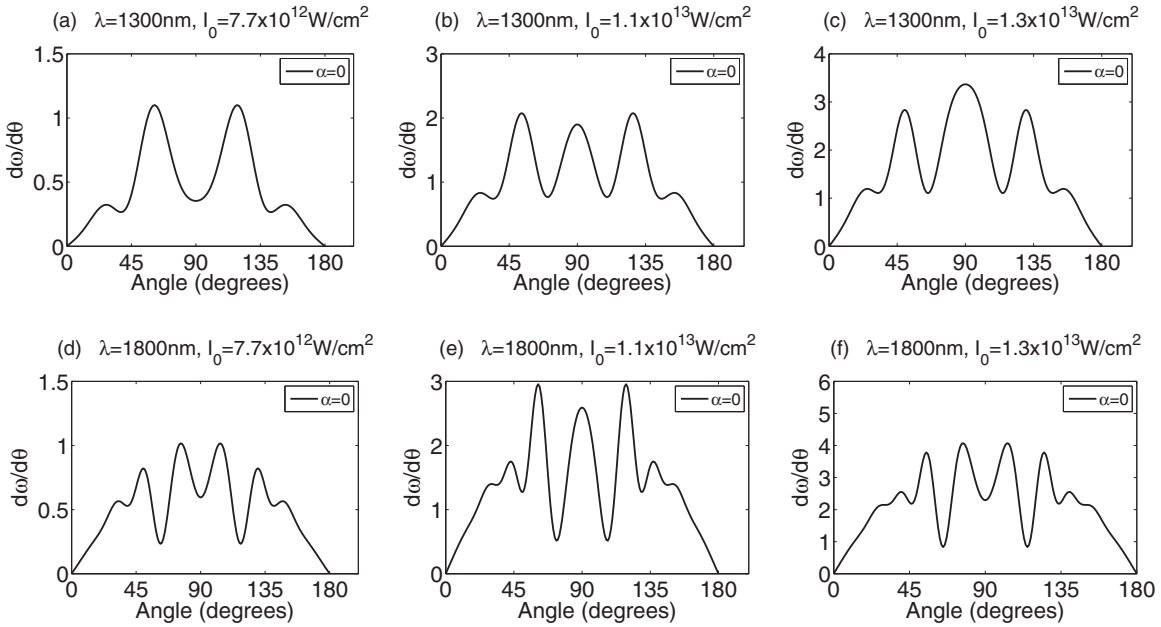

FIG. 5. Dependence of the photoelectron angular distribution on the n photodetachment channel with the CEP $\alpha = 0$. The panels in each row correspond to the peak laser intensities 7.7×10^{12}, 1.1×10^{13}, and 1.3×10^{13} W/cm^2. The panels in each column represent wavelengths of 1300 and 1800 nm. (a) shows five-photon detachment and (b) and (c) show six-photon detachment. (d), (e), and (f) show nine-, ten-, and eleven-photon detachment channels, respectively.

increased number of higher-order detachment channels and thus more detailed structure is recorded in the distributions. Comparison of Figs. 2(a), 2(b), and 2(c) at $\lambda = 1300$ nm and 2(d), 2(e), and 2(f) at $\lambda = 1800$ nm shows that the yield along each ring is strongly correlated with the direction of emission. Inspection of Figs. 2(a)–2(f), shows that the maxima of the rings occur along the direction of polarization while the minima of the rings for emission occur approximately perpendicular to the laser polarization. Our observations are in qualitative agreement with [22].

As in [22] the regular grid of sharply defined interference peaks in momentum space in combination with the radial interference rings observed in Figs. 2(a)–2(f) can be interpreted as a far-field continuum "quantum carpet" [28]. The origin of the interferences noted in Figs. 2(a)–2(f) may be explained by the fact that for direct electrons and a few-cycle pulse

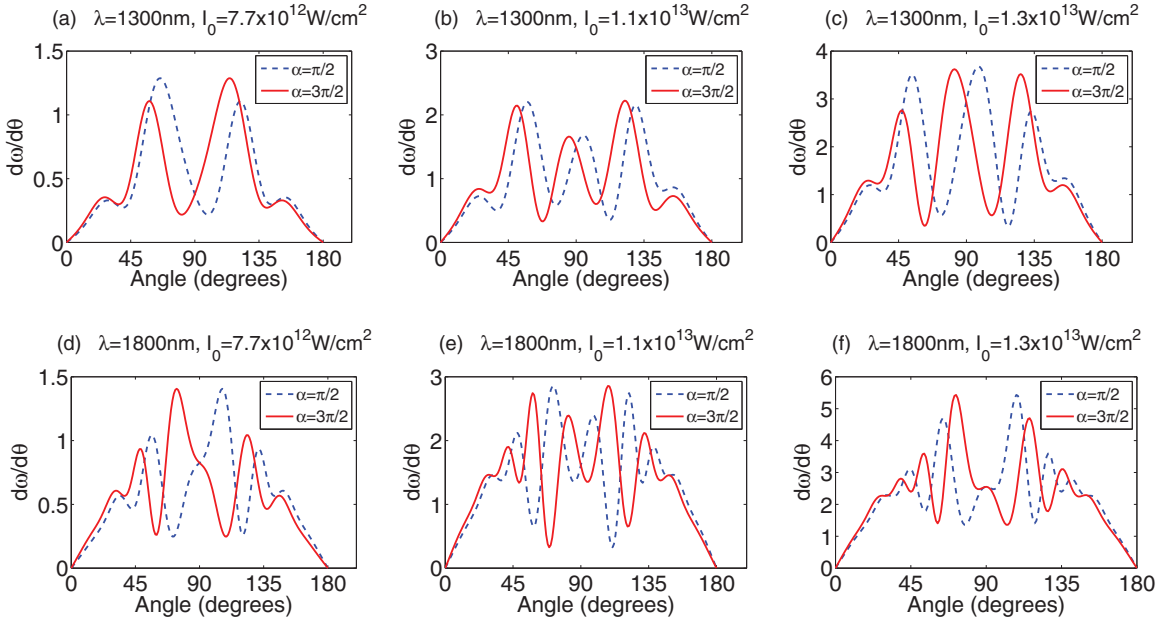

FIG. 6. (Color online) Dependence of the photoelectron angular distribution on the n photodetachment channel with the CEP $\alpha = \pi/2, 3\pi/2$. The panels in each row correspond to the peak laser intensities 7.7×10^{12}, 1.1×10^{13}, and 1.3×10^{13} W/cm^2. The panels in each column represent wavelengths of 1300 and 1800 nm. (a) shows five-photon detachment and (b) and (c) show six-photon detachment. (d), (e), and (f) show nine-, ten-, and eleven-photon detachment channels, respectively.

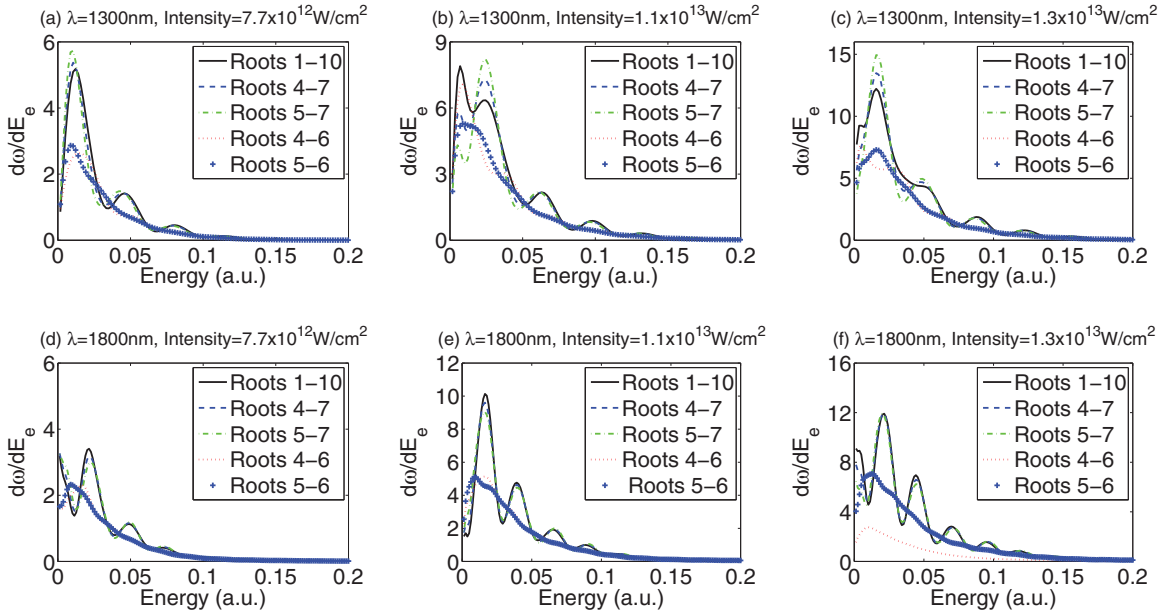

FIG. 7. (Color online) Photoelectron energy spectra calculated for a CEP of $\alpha = 0$ by including different numbers of saddle points in the amplitude: two (5 and 6) shown by blue plus signs, three (4–6) shown by the red dotted line, three (5–7) shown by the green dash-dotted line, four (4–7) shown by the blue dashed line, and ten (1–10) shown by the black solid line. The panels in each row represent laser intensities of 7.7×10^{12}, 1.1×10^{13}, and 1.3×10^{13} W/cm^2. The panels in each column correspond to laser wavelengths of 1300 and 1800 nm.

with a sine-squared envelope as described in Eq. (2) with N cycles there are exactly $2(N + 1)$ instants when the electron is detached throughout the duration of the laser pulse. These complex instants of time are start times of the electron (quantum) orbits in the presence of the laser field. Each of their contributions adds to the transition amplitude. This results in the radial interference effects caused by the corresponding wave packets. As reported in [22] we similarly observe that the perpendicular radial interference pattern in our distributions is generated by photodetachment at the two peaks of the laser field per intracycle time and this produces a 2ω energy separation of the ATD rings.

A notable feature in Figs. 2(a)–2(f) shows that the ATD peaks for an n-photon detachment channel get narrower as the threshold for absorption of additional photons increases at the onset of the continuum.

Further comparison with (i) strong-field approximation (SFA) calculations [22] for both (a) an infinitely long pulse and (b) a cosine-squared pulse with total pulse duration of 18 optical cycles and (ii) full numerical time-dependent Schrödinger equation (TDSE) simulations [22] is made. This shows that our calculations yield closer qualitative agreement with the TDSE results than with the analytical SFA calculations which neglect the effect of fine structure splitting. It should be noted that TDSE calculations automatically include the rescattered electrons, in contrast to both our calculations and the SFA calculations in [22]. This confirms that rescattering does not play a significant role in the energy regime considered here. Examination of Fig. 2 in [22] and the left-hand panel of Fig. 3 of [22] reveals a clear center which differs from our current results in Fig. 2(d). This qualitative discrepancy may be reconciled by noting that the calculations in [22] are based on employing the Hartree wave function for the initial state of F^-, which does not yield the correct asymptotic behavior. By contrast our initial-state wave function is asymptotically correct. It has been demonstrated in [29,30] that the use of asymptotically correct initial-state wave functions is very important for obtaining a correct description of above-threshold detachment in negative halide ions. Additionally, the results in Fig. 2 of [22] were obtained by the SFA for an infinitely long flat pulse. Another significant difference between the calculation in the left-hand panel of Fig. 3 in [22] and our present calculation is that the envelope used in our model is defined for a vector potential with a sine-squared pulse with shorter total duration of four optical cycles whereas the authors in [22] have specified the laser pulse in terms of the electric field using a cosine-squared pulse for 18 optical cycles. Inspection of Fig. 2 and and the left-hand panel of Fig. 3 of [22] in comparison with our Fig. 2 indicates that the interference structures are more sharply resolved for longer pulses than for short femtosecond laser pulses as considered here.

A notable general trend observed for both wavelengths is that the momentum distributions are symmetric about both $p_x = 0$ and $p_z = 0$ when the CEP $\alpha = 0$. For CEP values of $\alpha = \pi/2$ and $\alpha = 3\pi/2$ the momentum distributions retain their symmetry about the p_x axis only. It may be noted from Figs. 2(b) and 2(e) that for the distribution with a CEP of $\alpha = \pi/2$ the photoelectrons are more likely to be ejected in the backward direction, whereas Figs. 2(c) and 2(f) show that for a CEP of $\alpha = 3\pi/2$ the electrons are more likely to be ejected in the forward direction. Further comparison of Figs. 2(b) and 2(c) at $\lambda = 1300$ nm and Figs. 2(e) and 2(f) at $\lambda = 1800$ nm shows that there is mirror-image asymmetry between the forward direction α and the backward direction $2\pi - \alpha$. This observation that the asymmetry in the forward-backward (postive-negative) momentum distributions is CEP dependent is consistent with results reported [21,23] for angularly resolved electron spectra of H^- detached by short

infrared laser pulses. It is also noted from Figs. 2(b), 2(c), 2(e), and 2(f) that the structure of concentric rings is more clearly resolved for forward-backward-asymmetric distributions than for the symmetric case. In the forward direction for a fixed CEP of $\alpha = \pi/2$ it is observed that the interference is weaker than in the backward direction. For a fixed CEP of $\alpha = 3\pi/2$ the distributions in Fig. 2 show that the interference effects are more pronounced in the forward direction. Thus these results show that the CEP is a useful tool in controlling the behavior of the interference structures observed in photodetachment of F^- ions by few-cycle laser pulses.

The momentum maps for F^- ions shown here are quite different physically from those obtained for H^- ions in [21,23], which are characterized by a set of above-threshold detachment peaks, in contrast to the above-threshold concentric rings observed for F^- ions. This difference may be accounted for by the fact that the calculations for H^- ions in [21,23] were carried out for an $l = 0$ ground state, whereas the present calculations for F^- ions are carried out for an $l = 1$ ground state. This indicates that the structure of the low-energy momentum maps considered in both cases, whose spectra include only the contribution of direct electrons, is strongly dependent on the parity of the negative ground-state ion. Finally it should be noted the momentum maps in Figs. 2 and 3 include the $m = 0, +1$ and $m = -1$ state components of the initial p state of the F^- ion. We report that additional simulations of the momentum maps carried out (not shown here) show that neglect of the $m = -1$ and $m = +1$ states leads to a significant underestimation of the momentum distributions and do not capture the complete physical picture of constructive and destructive interference effects.

C. Photoelectron differential detachment probability

In Fig. 4 we display some sample spectra of photoelectron differential detachment probabilities for a four-cycle pulse at laser intensities of 7.7×10^{12}, 1.1×10^{13}, and 1.3×10^{13} W/cm^2 for the p states of above-threshold detachment for the F^- ion. The detachment probabilities at each intensity are investigated by using two laser wavelengths of 1300 and 1800 nm for a fixed CEP of $\alpha = 0$ in the vicinity of channel closings.

In particular Fig. 4(a) corresponds to five-photon detachment, Figs. 4(b) and 4(c) yield a six-photon detachment channel, Fig. 4(d) corresponds to nine-photon detachment, Fig. 4(e) shows a ten-photon detachment channel, and Fig. 4(f) depicts an eleven-photon detachment channel.

Comparison of Figs. 4(a)–4(f) shows that the probability of detachment at a fixed wavelength of either 1300 or 1800 nm increases with increasing intensity. We also observe that at each fixed intensity as the wavelength increases the probability of electron detachment also increases. These calculations include the contribution of the $m = 0$, $m = +1$, and $m = -1$ components to the photoelectron emission in the ground state. While the $m = 0$ component of the initial p state gives the dominant contribution to the detachment probabilities, neglect of the $m = +1$ and $m = -1$ spinor-spherical harmonics leads to a significant underestimation of the detachment probabilities in the present model. Calculations carried out by Kiyan and Helm [1] adopting the GK theory [6] for a long periodic pulse show very good qualitative agreement with our data at 1800 nm for a long laser pulse of 1.1×10^{13} W/cm^2. Comparison of our predictions with [1] reveals close similarity of the nonmonotonic structure of their spectra. The two additional smaller peaks that occur in our spectra but not in [1] are a manifestation of the few-cycle laser pulse.

In accord with the predictions of Bergues *et al.* [4] we find that in our model saturation effects are negligible at the lower laser intensities of 7.7×10^{12} and 1.1×10^{13} W/cm^2 but begin to have a stronger influence at 1.3×10^{13} W/cm^2. Additional calculations carried out at higher intensities of 1.7×10^{13} and 3.4×10^{13} W/cm^2 (not reported here) for both wavelengths of 1300 and 1800 nm show that the saturation effects become increasingly significant in determining the profile of the spectra, as depletion of the negative ions at the leading front of the laser becomes more critical at higher intensities and thus can no longer be neglected in the ground state in our model. Comparison of our spectra with the results of [4] shows that the main feature of the nonmonotonic oscillatory structures are qualitatively well reproduced in the present calculations. At the higher wavelength of 1300 nm and stronger intensities of 1.1×10^{13} and 1.3×10^{13} W/cm^2 it is noticeable that the F^- ions contribute to narrower energy peaks in contrast to the results at the lower wavelength of 1300 nm where they spread over several broader excess photodetachment peaks.

Similar trends are noted (not shown here) for probability distributions calculated with CEP values of $\alpha = \pi/2$ and $3\pi/2$. The symmetrical properties of the distributions are dependent on the CEP, being symmetric at $\alpha = 0$ and asymmetric for $\alpha = \pi/2$ and $3\pi/2$. These findings indicate that the CEP is an additional laser control parameter that can steer the behavior of the detached electron in the photodetachment process. The distributions in Figs. 4(a)–4(f) show clearly that the threshold for photodetachment is strongly dependent on both increasing laser intensity and increasing laser wavelength. The shape of each of the distributions is strongly characterized by the above-threshold detachment peaks which are a feature of channel-closing-induced bifurcation effects. This behavior has been observed in previous calculations for negative ions whose initial state has s symmetry [11,21]. In addition, the Sturmian-Floquet predictions for threshold effects in [11] of negative ions with initial p-electron symmetry are confirmed by our results.

D. Photoangular distributions

In order to obtain a deeper insight into the threshold behavior of PADs near channel closings we analyze their dependence in Figs. 5 and 6 on laser wavelength, intensity, and CEP for the p bound state of F^- exposed to a four-cycle laser pulse. Comparison of Fig. 5(a) with Fig. 5(b) shows that there is a critical bifurcation peak laser intensity I_0 [defined as in Eq. (3)] in the range $7.7 \times 10^{12} < I_0 < 1.1 \times 10^{13}$ W/cm^2 at which the fifth photon detachment channel closes. The four-peak structure in Fig. 5(a) which is connected by three minima is transformed into a five-peak structure connected by four minima at the stronger intensity of 1.1×10^{13} W/cm^2 in Fig. 5(b). This corresponds to a six-photon detachment channel. Direct comparison of Fig. 5(b) with Fig. 5(c) shows that at the higher intensity in Fig. 5(c) the maximum of

the middle peak is now much higher and broader than the maxima of the two peaks on either side of it, reversing the trend observed in Fig. 5(b). The magnitudes of all five peak structures in Fig. 5(c) have also increased significantly. This profile coincides with the six-photon detachment channel in Fig. 5(c) approaching threshold behavior near its channel closure. It is noted in Figs. 5(a)–5(c), that the maxima of the outermost peaks are of much smaller magnitude than the innermost peaks.

In Fig. 5(d) corresponding to nine-photon detachment there is a distinct signature of six peaks. Similarly the tenth and eleventh photon detachment channels depicted in Figs. 5(b) and 5(c) are characterized by unique signatures of seven and eight peaks, respectively. As in Figs. 5(a)–5(c) it is observed that the heights of the peaks for each detachment channel at the fixed laser wavelength of 1800 nm increase with increasing intensity. Further analysis of Figs. 5(a)–5(f) also demonstrates that the maxima of the lowest peaks become washed out and they evolve into a flat-shouldered plateau as the intensity increases. The bifurcation phenomenon which is a feature of channel closure in Figs. 5(a)–5(f) is governed by increase of the ponderomotive shift $U_p = F_0^2/4\omega^2$. The critical bifurcation intensity and wavelength for n-photon detachment for a short pulse are determined from the law $E_e \approx n\omega - U_p - |E_0|_j$ and occur close to $E_e \to 0$, where E_e is the final kinetic energy of the detached electron and $|E_0|_j$ (with $j = 1/2$) the bound-state energy of the F^- ion.

Comparison of the plots in Figs. 5(a)–5(f) illustrates that with the CEP $\alpha = 0$, the PADs for the odd photon channels considered here ($n = 5,9,11$) are distinguished by a minimum in the direction of laser polarization but the PADs for even photon detachment channels ($n = 6,10$) are characterized by a maximum located along the polarization direction of the laser field. This pattern of electron emission for even- and odd-n PADs was also found in the study [21,24] of H^-, which indicates that this particular characteristic of the PADs is independent of the initial-state symmetry.

Our results show that for F^- with initial orbital angular momentum $l = 1$, if an odd number of photons is absorbed, the distributions have an even number of peaks, while if an even number of photons is absorbed, the distributions have an odd number of peaks. Similar observations were made in [11,21] in H^- for an s ground state for two- and three-photon detachment but the topologies of the structures are qualitatively different, indicating that the geometrical structure of the PADs is sensitive to the initial-state symmetry of the active electron.

Next we study the effect of the CEP dependence of PADs for a laser wavelength of 1300 nm and intensities of 7.7×10^{12}, 1.1×10^{13}, and 1.3×10^{13} W/cm^2. In Figs. 5(a)–5(f) we see that for each intensity considered the PADs are symmetric about 90° for a CEP of $\alpha = 0$. Comparison with Figs. 6(a)–6(f) shows that the PADs calculated at $\alpha = \pi/2$ are shifted to the right of the $\alpha = 0$ distributions and the PADs calculated for $\alpha = 3\pi/2$ are shifted toward the left of the $\alpha = 0$ distributions. The positions of the maxima and minima in the jetlike structures in Figs. 6(a)–6(f) are observed to be highly dependent on the CEP.

The distributions for $\alpha = \pi/2$ are the mirror images of those at $3\pi/2$ about 90° along the angular axis for the three laser intensities considered. This shows that the photodetachment probabilities in the forward direction of $\alpha = \pi/2$ are equal to those in the backward direction $\alpha = 3\pi/2$. The wavelength dependence of this asymmetry is also noted in Fig. 6. With increasing wavelength at a fixed laser intensity the corresponding asymmetry amplitudes in Figs. 6(a)–6(f) yield a higher value than the corresponding symmetric amplitudes considered in each case in Fig. 5. It is further noted from Figs. 5 and 6 that for a fixed wavelength with increasing intensity the amplitudes of the oscillatory peaks for both the symmetric and asymmetric PADs increase.

These results in this section show that the degree of asymmetry and the structures in the PADs are highly sensitive to variation in the CEP. Thus measuring such distributions provides a robust tool for determining this phase in multiphoton detachment of negative ions where in the initial state the electron's orbital angular momentum has p symmetry.

E. Photoelectron energy spectra

We now consider threshold effects in the photoelectron energy spectrum of the negative F^- ion near channel closure. The dominant characteristic of the spectra in Figs. 7(a)–7(f) is a clear structure of above-threshold peaks corresponding to a multiphoton mechanism, where each peak is separated approximately from its nearest neighbor by the photon energy ω, as for a short pulse $E_e + U_p + |E_0|_j \approx n\omega$ for some integer n. These peaks are wider (as expected [20,21]) than is the case for a long laser pulse, due to the combined wave-packet interference effects from the $2(N + 1)$ saddle-point contributions, over the duration of the short laser pulse. Figure 7(a) shows the five-photon detachment channel and Figs. 7(b) and 7(c) are the results for six-photon detachment channels. Figures 7(d), 7(e), and 7(f) show the calculations for nine-, ten-, and 11 eleven-photon detachment channels, respectively. From Figures 7(a)–7(f) it is observed that as the ponderomotive shift is increased with increasing intensity and wavelength the number of prominent excess photon detachment channel increases, corresponding to the absorption of many more photons than necessary at the onset of the continuum. It is noted from Figs. 7(a)–7(f) that an increase in higher-order detachment channels is accompanied by increasing probability of closure of the lower-order channels. This happens because as the ponderomotive potential raises the continuum threshold the minimum number of photons required to detach an electron from a negative ion increases when the laser intensity and/or wavelength is increased. This leads to closure of lower photon detachment channels. Our results show that the threshold for photodetachment increases as the ponderomotive shift increases.

In Fig. 7 we analyze how the behavior of the energy spectrum is influenced by the number of saddle points included in the evaluation of the transition amplitude. It can be seen from Fig. 7 that at the lower wavelength of 1300 nm all ten saddle points need to be included to obtain the complete spectrum, as compared with the calculations for $\lambda = 1800$ nm, where Figs. 7(d)–7(f) show that only roots 4–7 need to be included to give accurate results. This is because at $\lambda = 1300$ nm the laser field is weaker than at $\lambda = 1800$ nm for the range of laser intensities considered here. At the higher wavelength roots 5–7 give the dominant contribution to the transition amplitude. This is consistent with the results in [20], where it was also found

that at lower wavelengths all saddle points need to be included. This indicates that at lower electron energies and wavelengths, the saddle points further from the real axis play a stronger role than at higher wavelengths and electron energies. Similar behavior was noted in [21].

The limit of applicability of our adiabatic saddle-point approach can be determined from the Keldysh parameter $\gamma = \frac{\omega\kappa}{F_0}$ where ω, κ, and F_0 have been defined in Sec. II. The multiphoton regime requires that $\gamma \geqslant 1$ and the tunneling regime requires $\gamma < 1$. Here $\gamma = 1.192$, 0.998, and 0.918 at $\lambda = 1300$ nm for laser intensities of 7.7×10^{12}, 1.1×10^{13}, and 1.3×10^{13} W/cm^2, respectively. At the higher wavelength of 1800 nm considered, the Keldysh parameter satisfies $\gamma < 1$ (i.e., $\gamma = 0.8615$, 0.7208, and 0.6631 for increasing laser intensities of 7.7×10^{12}, 1.1×10^{13}, and 1.3×10^{13} W/cm^2, respectively). The present results in Fig. 7 indicate that the multiphoton mechanism is dominant for the range of laser parameters considered in this paper, despite the Kelydsh theory predicting that when $\gamma < 1$ the photodetachment dynamics are governed predominantly by tunneling. It should be noted that in our calculation the effect of averaging over the spatial laser inhomogeneity to take account of the radial dependence of the intensity has not been considered. As shown by Reiss [31] this modification might be expected to cause the multiphoton peaks in Fig. 7 to disappear and be replaced by continuous energy spectra characteristic of the tunneling regime expected at higher intensities and longer wavelengths. However Reiss [31] explained that the inclusion of spatial laser inhomogeneity yielding a smoother distribution does not necessarily mean that the spectra may be interpreted as indicating a tunneling mechanism. This is because the spatial integration over the the intensity distribution is physically a superposition of many different photon orders and the contributions from different orders overlap and result in continuous spectra. The present calculations highlight an apparent contradiction in the multiphoton-tunneling dichotomy if interpreted very strictly, according to whether the Keldysh parameter γ is greater than or less than unity. The present results in Fig. 7 show that $\gamma < 1$ does not necessarily preclude the multiphoton mechanism for the range of laser parameters considered here. Our calculations here show that a few-cycle laser pulse can produce $2(N + 1)$ photoelectron wave packets and guide them through different multiphoton pathways in the continuum, thus controlling the interference effects in the various multiphoton detachment electron spectra as observed in Figs. 7(a)–7(f).

Additional calculations carried out but not reported here show that the electron energy spectrum is CEP controlled. The contribution of individual saddle points to the energy spectra is directly determined by the value of the CEP. Our calculations show that increasing either the wavelength or intensity causes the low-energy peaks to vanish. In particular we have seen that the properties that evolve with increasing laser intensity or wavelength or variation of the CEP of the energy spectra serve as useful diagnostic probes of the photodetachment dynamics of channel closure at threshold.

IV. CONCLUSIONS

We have extended the adiabatic saddle-point method in [20,21] to direct photodetachment of F^- electrons by mid-infrared short (femtosecond) linearly polarized laser pulses in the multiphoton regime. In particular the model can be used to investigate threshold effects. We have considered the behavior of the photoelectron momentum saddle points (p_x, p_z) in the upper half plane of complex t and found that they are highly sensitive to variation in (i) laser wavelength, (ii) laser intensity, and (iii) CEP.

Analysis of the momentum distribution probability maps of photoelectron spectra reveals a remarkably detailed concentric-ring structure of above-threshold detachment, attributed to quantum wave-packet interference effects arising from $2(N + 1)$ saddle points, emitted at various complex-valued moments of time. The distinctive complex patterns produced by these momentum maps are consistent with the predictions of [22]. Further comparison of these results with those for H^- in [21] demonstrates the importance of the initial-state symmetry of the active electron. It has been noted that as the wavelength increases at fixed intensity, the number of concentric rings increases due to increase in the number of photodetachment channels. It has further been observed that the momentum distributions in the forward direction for a CEP α are identical to those in the backward direction for $2\pi - \alpha$. Thus controlled CEP-dependent asymmetry provides a powerful tool for extracting information about the mechanism underlying photodetachment on a femtosecond time scale.

Calculated detachment probability distributions predict the oscillatory behavior expected from quantum interference effects due to coherent electronic wave-packet dynamics. Comparison of these results with those of [20,21] shows that a similiar trend was noted for H^-. The geometrical structure of the probability distributions is determined by bifurcation effects which occur in the region of multichannel photon closure. These distributions indicate that the threshold for each higher-order individual n-photon detachment channel is governed directly by increasing laser wavelength and increasing intensity. Additionally these distributions exhibit sensitivity to CEP control as a function of both laser intensity and wavelength.

The formation of near-threshold structures in the PADs for n-photon absorption (for $n = 5$, 6, 9, 10, and 11) in the vicinity of channel closings has been probed. Variation of the PADs as a function of laser wavelength and intensity has been found to be strongly dependent on the initial-state symmmetry. These findings are in qualitative agreement with predictions of the Floquet-Sturmian theory [11] and the Keldysh saddle-point approach [6]. Additionally the PADs of the electron spectra exhibit strong asymmetric dependence on the CEP. The angular distributions calculated in opposite directions ($\alpha = \pi/2$, $\alpha = 3\pi/2$) depict forward-backward asymmetry and the resulting distributions are mirror images of each other. Accordingly, since optimal emission of photoelectrons varies with CEP, control of the photoelectron angular distributions can be obtained by steering electrons via this parameter. Our calculations further show that control of the PADs can be achieved by manipulating the ponderomotive shift. This parameter dominates the shape of the PADs and plays a crucial role in determining the threshold for n-photon detachment.

We have shown that the photoelectron energy spectra consist of a structure of pronounced oscillatory peaks due to above-threshold detachment, a correlated process, where the

final-state energy of the detached electron is constrained to integer multiples of the photon energy above the ponderomotive-shifted ground state. The peaks are due to quantum interference effects caused by the $2(N+1)$ saddle-point contributions to the photodetachment amplitude. The photoelectron energy spectra are also found to be sensitive to variation of the CEP.

Future directions for applications and extensions include extending this model to incorporate the rescattering mechanism in order to consider the high-energy regime which was not taken into account in this paper. It would also be very interesting to extend this model to consider electron detachment in the Si^- negative ion, which is an open-shell system, and compare with any available existing experimental data. This work may also be of use to experimentalists in combining a pump-probe approach with CEP control technology to study electronic quantum interference in halide negative molecular ions.

ACKNOWLEDGMENT

The authors gratefully acknowledge very useful and fruitful discussions with Dr. Gleb Gribakin.

[1] I. Yu. Kiyan and H. Helm, Phys. Rev. Lett. **90**, 183001 (2003).
[2] J. Pedregosa-Gutierrez, P. A. Orr, J. B. Greenwood, A. Murphy, J. T. Costello, K. Zrost, T. Ergler, R. Moshammer, and J. Ullrich, Phys. Rev. Lett. **93**, 223001 (2004).
[3] H. R. Reiss, Phys. Rev. A **76**, 033404 (2007).
[4] B. Bergues, Z. Ansari, D. Hanstorp, and I. Yu. Kiyan, Phys. Rev. A **75**, 063415 (2007).
[5] B. Bergues and I. Yu. Kiyan, Phys. Rev. Lett. **100**, 143004 (2008).
[6] G. F. Gribakin and M. Yu. Kuchiev, Phys. Rev. A **55**, 3760 (1997).
[7] M. V. Frolov, N. L. Manakov, E. A. Pronin, and A. F. Starace, Phys. Rev. Lett. **91**, 053003 (2003).
[8] D. B. Milosevic, A. Gazibegovic-Busuladzic, and W. Becker, Phys. Rev. A **68**, 050702(R) (2003).
[9] S. Beiser, M. Klaiber, and I. Y. Kiyan, Phys. Rev. A **70**, 011402(R) (2004).
[10] A. Gazibegovic-Busuladzic, D. B. Milosevic, and W. Becker, Phys. Rev. A **70**, 053403 (2004).
[11] K. Krajewska, I. I. Fabrikant, and A. F. Starace, Phys. Rev. A **74**, 053407 (2006).
[12] A. Gazibegović-Busuladžić, D. B. Milošević, and W. Becker, Opt. Commun. **275**, 116 (2007).
[13] A. Gazibegovic-Busuladzic, D. B. Milosevic, W. Becker, B. Bergues, H. Hultgren, and I. Y. Kiyan, Phys. Rev. Lett. **104**, 103004 (2010).
[14] B. Fetić, D. B. Milošević, and W. Becker, J. Mod. Opt. **58**, 1149 (2011).
[15] S. Bivona, G. Bonanno, R. Burlon, and C. Leone, Phys. Rev. A **76**, 021401(R) (2007).
[16] S. Bivona, G. Bonanno, R. Burlon, D. Gurrera, and C. Leone, Phys. Rev. A **77**, 051404(R) (2008).
[17] S. Bivona, G. Bonanno, R. Burlon, and C. Leone, Laser Phys. **19**, 805 (2009).
[18] B. Li-Hua, H. Lu-Qiang, C. Ting-Ting, L. Yu-Heng, W. Yan, Z. Hui-Fang, and D. Dong-Mei, Chin. Phys. Lett. **28**, 063202 (2011).
[19] D. M. Volkov, Z. Phys. **94**, 250 (1935).
[20] S. F. C. Shearer, M. C. Smyth, and G. F. Gribakin, Phys. Rev. A **84**, 033409 (2011).
[21] S. F. C. Shearer and C. R. J. Addis, Phys. Rev. A **85**, 063409 (2012).
[22] Ph. A. Korneev, S. V. Popruzhenko, S. P. Goreslavski, W. Becker, G. G. Paulus, B. Fetić, and D. B. Milošević, New J. Phys. **14**, 055019 (2012).
[23] L.-Y. Peng, Q. Gong, and A. F. Starace, Phys. Rev. A **77**, 065403 (2008).
[24] J. Zhang, W. Zhang, Z. Xu, X. Li, P. Fu, D.-S. Guo, and R. R. Freeman, J. Phys. B **35**, 4809 (2002).
[25] I. S. Gradshtein and I. M. Ryzhik, *Tables of Integrals, Series, and Products* (Academic Press, Boston, 1994).
[26] T. Andersen, H. K. Haugen, and H. Hotop, J. Phys. Chem. Ref. Data **28**, 1511 (1999).
[27] E. E. Nikitin and B. M. Smirnov, *Atomic and Molecular Processes* (Nauka, Moscow, 1988).
[28] A. E. Kaplan, I. Marzoli, W. E. Lamb, Jr., and W. P. Schleich, Phys. Rev. A **61**, 032101 (2000).
[29] G. F. Gribakin, V. K. Ivanov, A. V. Korol, and M. Yu. Kuchiev, J. Phys. B **32**, 5463 (1999).
[30] G. F. Gribakin, V. K. Ivanov, A. V. Korol, and M. Yu. Kuchiev, J. Phys. B **33**, 821 (2000).
[31] H. R. Reiss, Phys. Rev. A **75**, 031404(R) (2007).